Global analysis of the influence of contacts on Heusler–based thermoelectric modules

G.Roy[1,*], C.van der Rest[1], S.Heymans[1], E.Quintin[1], V.Dupont[2], J.P.Erauw[2] , A.Schmitz[3], P.J.Jacques[1]

1-Université catholique de Louvain, Institute of Mechanics, Materials and Civil Engineering, Materials and process engineering (IMAP), Place Sainte Barbe 2, B-1348 Louvain-la-Neuve, Belgium

2- Belgian Ceramic Research Center (BCRC), avenue Gouverneur Cornez 4, B-7000 Mons, Belgium

3- CRM Group, avenue du Bois Saint Jean 21, B-4000 Liège, Belgium

**- e-mail :geoffrey.roy@uclouvain.be*

The interest for waste heat recovery using thermoelectricity grew up in the last decades. Up to now, most researches and developments focused on high performances and/or low cost materials. However, for practical applications, modules based on these materials are needed. This work presents the development and optimisation of modules based on the low cost Fe_2VAl Heusler compound. It depicts a global analysis of the assembly relating the microstructure of the joint, the contact resistances and the module performances. Based on this analysis, a generic method for developing joining solutions for new thermoelectric materials is proposed. Using this method, the diffusion bonding technique leading to an electrical contact resistance of 5 10^{-9} $\Omega.m^2$ was highlighted and a thermoelectric module with a power density higher than 500 $W.m^{-2}$ for a temperature difference of 200 K has been developed.

Key words: Thermoelectric module, Heusler, electrical contact, thermal contact

INTRODUCTION

In recent years, thermoelectric generators (TEG) have gained interest for waste heat harvesting. While most research focuses on the optimisation of material performances, major challenges remain at the level of the complete setup, that still restrain the use of thermoelectricity to niche applications [1]. Especially, the assembly of the constitutive elements of TEG, *p*- and *n*-type materials, electrical and thermal conductors and insulators intrinsically leads to contact resistances that hinder the performances of TEG [2]. As shown in Figure 1, these contacts that correspond to each interface between different materials influence the electrical and/or thermal performances. Previous studies on thermoelectric contacts mostly focused on either the optimisation of the metal to semiconductor contact (related to the microstructure of different types of thermoelectric materials [3, 4, 5]) or on the influence of contact resistances at the system level [6-11], which are only parts of the global issue. Recently, Ngan *et al.* [12] studied the relationship between contact resistance and microstructure. However, they only estimated theoretically the influence of this relationship on the system efficiency. In order to widespread the use of new thermoelectric materials in practical applications, the up-scaling from one single contact to a complete TEG should be experimentally investigated. This step is mandatory to validate the repeatability and the scalability of the joining method. It seems that none of these studies proposed a global approach relating experimentally the microstructure of the joints to the contact resistance and the performances at the TEG level, even though this global view could accelerate the development of new optimised thermoelectric devices based on innovative materials.

The present study aims at applying this global methodology to optimise a TEG based on a thermoelectric material well suited for large-scale waste heat harvesting applications [13]. Indeed, Fe_2VAl compound, firstly studied by Nishino *et al.* [14, 15, 16] is based on low-cost elements and presents a high power factor (up to 6.8 10^{-3} $W.m.K^{-2}$). Moreover, adequate doping or decrease of the grain size lead to a significant decrease of the thermal conductivity, leading to *ZT* values around 0.2 in the 400-500 K range [17, 18]. Finally, the Fe_2VAl compounds present processing and manufacturing properties very close to metallic materials, which is also a large advantage for large-scale applications.

Different joining techniques were tested and characterised both by looking at the microstructure and at the resulting electrical properties. Their performances in fully working prototypes are discussed using a lumped model that highlights the relationship between microstructure and system performances. It gives guidelines for the enhancement of system performances.

EXPERIMENTAL PROCEDURE

Thermoelectric materials

The Fe_2VAl thermoelectric material used in this work has been processed by induction melting of ferrovanadium, iron and aluminium pellets followed by a slow cooling stage (10 $K.min^{-1}$) to avoid cracks and solidification defects. Ferrovanadium is used instead of pure vanadium because of its much lower cost without hindering the thermoelectric performances. The doping strategy is based on off-stoichiometry optimisation following the formula $(Fe_{2/3}V_{1/3})_{100-y}Al_y$. Indeed, varying the aluminium concentration allows to switch from *n*-type to *p*-type materials [14]. The amount of each of the constituents needed to reach the right stoichiometry were placed in a boron nitride crucible then heated up to 1960 K under vacuum during 20 min before being slowly cooled (10 $K.min^{-1}$). The resulting ingots weight around 100 g. Compositions of the base materials and of the melted samples were compared. A slight loss of Al and V (below 0.5 at.%) was observed due to the precipitation of nitrides and carbides [19]. Table I summarises the actual compositions measured by inductively coupled plasma atomic emission spectroscopy. Boron nitride crucibles were used in order to limit C contamination during the melting process. Values lower than 0.15 wt.% C were measured on the processed samples and it was shown that it has no influence on the Seebeck coefficient [19].

Joining processes

A good joint must present an adequate chemical reactivity between the thermoelectric material and the metal junction in order to bring a good mechanical strength while avoiding the formation of brittle intermetallic compounds at the interface that would lead to a higher surface contact resistivity [1]. Furthermore, it can be postulated that a smaller joint thickness leads to a smaller surface contact resistivity. In this work, copper has been selected for the metallic junctions. This choice is motivated by the fact that it has been previously demonstrated that copper can perform up to 673 K and resist to thermal cycling in Fe_2VAl-based TEG [20,21].

The different joining solutions have been carried out on 0.7 mm thick copper sheets. The Fe_2VAl samples were machined into 5x5x5 mm cubes. Copper and Fe_2VAl have been slightly polished with SiC paper and degreased with ethanol before every joining process. Four different techniques were tested to join the thermoelectric Fe_2VAl blocks with copper connecting sheets. Conductive silver glue, tin solder, silver braze and diffusion bonded copper were considered in the present study. In contrast with commercial thermoelectric modules where solders based on tin-bismuth alloys are widely used [9], other techniques have to be studied here since the nature of the materials and the expected operating temperature range (up to 673 K [13]) are significantly different. Even though they do not allow reaching such high temperatures, silver glue and tin solder were tested since they are quite conventional solutions, somehow widely used in other applications [22]. Silver brazing has been successfully used for iron aluminide joining [23]. Since it gives low wetting angles, this technique seemed promising for Fe_2VAl-Cu joining. Since copper presents a good wetting behaviour with iron aluminides [24], direct joining of copper to Fe_2VAl through diffusion bonding technique was also considered. Furthemore, this process has been used previously by Mikami *et al.* [20].

The silver glue is an epoxy-based glue containing micrometric silver particles. The glue used in this work is the 10HT/S from MasterBond. It has an intrinsic electrical resistivity lower than 2 $\mu\Omega$.m and a working temperature ranging from 4 K to 477 K. It was deposited by hand using a spatula. The curing stage consisted in a hold for 45 min at 418 K under ambient atmosphere. The Fe_2VAl-Cu assembly was furthemore pressed using a screwed assembly.

The tin solder used in this study, commercialised by Multicore, is a solder paste with a composition of 95.5 wt.% Sn, 3.8 wt.% Ag and 0.7 wt.% Cu. This paste presents a melting point around 490 K. The soldering cycle has been carried out with a holding time of 20 min at 540 K under ambient atmosphere in the same clamping assembly than for the silver glue.

The silver braze used is the 1666PA from Castolin. Its composition is 45 wt.% Ag, 27 wt.% Cu and 28 wt.% Zn. Its liquidus and solidus temperatures are 953 K and 913 K, respectively. The brazing cycle was conducted under vacuum (0.1 mbar) at 973 K for 15 min within a SRO-700 furnace from ATV Technologie.

For the diffusion bonding of Fe_2VAl and copper, the Fe_2VAl sample is pressed under 20 MPa between two copper sheets and heated up at $50K.min^{-1}$ to 1200 K for 2 min in a spark plasma sintering (SPS) device (HPD10, FCT Systeme).

Characterisation of the joints

The microstructure of the joints has been characterised by scanning electron microscopy (SEM) and energy-dispersive X-ray spectroscopy (EDX). The Fe_2VAl-Cu assemblies were cut in the center of the Fe_2VAl leg before being polished to observe the interface between copper and Fe_2VAl.

The total electrical resistance of the different joined samples, R_{meas}, was measured with a custom four-probe measurement setup. Knowing the internal resistance of the Fe_2VAl sample, R_{mat} derived from its geometry and the material electrical resistivity, the electrical contact resistivity, ρ_{sc} [Ω.m²], has been estimated as:

$$\rho_{sc} = (R_{meas} - R_{mat})A \quad (1)$$

with A is the contact area of the Fe_2VAl sample (25 mm² in this work).
This method is similar to the integral method proposed and validated by De Boor *et al.* [4].

Processing of prototypes

Four prototypes were fabricated based on different Fe_2VAl compounds and different joining techniques with a number of couples varying from 7 to 40. The lower copper plates were first properly placed in an array and a layer of joining material was deposited on it. The *p*-type legs were then placed followed by the *n*-type legs (or alternatively) and a layer of joining material was deposited on these legs. Finally, the upper copper plates were placed. Each prototype used copper plates of 5x12x0.7 mm. The different prototypes were:

- **A silver glue prototype**. For the assembly of this first prototype, a droplet of silver glue was placed on each Cu - Fe_2VAl interface by hand. Once the assembly was completed, it was heated up to 418 K for 45 min under ambient air.
- **A tin soldering prototype**. This second prototype was designed on the same scheme than the silver glue prototype. Owing to a larger number of couples with higher Seebeck coefficients and better electrical contact, better performances were expected from this prototype. The same steps as for the silver glue prototype were carried out with a heating stage at 540 K for 20 min.
- **A silver brazing prototype**. This prototype was designed to work at higher temperatures than the previous ones using the same Fe_2VAl compounds. For this prototype, the assembly was carried out on a graphite PAPYEX sheet (from MERSEN) in a SRO-700 furnace and an alumina plate was put on top of it. To ensure good contacts, a pressure of 17 kPa was applied on top of the assembly using a weight. The brazing cycle was carried out at 973 K for 15 min.
- **A copper diffusion bonded prototype**. The Fe_2VAl legs were joined to copper using the diffusion bonding technique previously presented. The assembly has then been carried out with silver brazing and pressure for copper-copper junctions as for the previous prototype.

The materials and geometrical properties of these prototypes are detailed in Table I. The geometry of the thermoelectric legs has been chosen to facilitate the machining process and the manual manipulation during the prototype assembly.

Measurements of the performances of the prototypes

Two types of measurements were carried out on the prototypes. Firstly, the internal electrical resistance (R_{meas}) was measured with a four-probe technique. Small currents (≤ 100 mA) were used to minimise the influence of the thermoelectric effect on the measurements. Secondly, the open circuit voltage (V_{oc}) for a given temperature difference between the cold side and the hot side of the TEG was measured on a custom setup schematically represented on Figure 2. In this setup, a finned heat sink is immersed in a controlled cooler allowing temperatures down to 233 K. The prototype is placed between the heat sink and an electrical heater (a 1 Ω-200 W rated power resistance) allowing heating the hot side up to 423 K. The heat sink and the heater casing are both made out of anodised aluminium. The anodised layers serve as insulator between the copper plates and the heat exchangers and allow avoiding the use of additional ceramic plates. Silicon thermal grease is used on both sides of the prototypes to ensure good thermal contacts. Screws clamp the prototypes between the heater and the heat sink to add some pressure and to ensure a good contact. Holes are drilled in the heat sink and the aluminium casing of the heater to measure hot and cold side temperatures with K-type thermocouples. Voltage is measured with a portable multimeter. It is worth noting that the silver glue prototype has been assembled and screwed between the heater and the heat sink before the curing step.

With the measurements of the open circuit voltage and the corresponding temperature difference, the effective Seebeck coefficient proposed by Huang *et al.* can be deduced using the following equation [25],[26]:

$$V_{oc} = \sum_{mat} \Delta T_{teg} = \sum_{meas} \Delta T \tag{2}$$

Where V_{oc} is the open circuit voltage, $\sum_{mat}=S_p-S_n$ is the material couple Seebeck coefficient in V.K^{-1}, ΔT_{teg} is the effective temperature difference on the thermoelectric legs, $\sum_{meas}$ is the effective Seebeck coefficient and ΔT is the temperature difference measured across the prototype.

Lumped model of the thermoelectric prototypes

To critically assess the influence of the thermal and electrical contact resistivities, a first order lumped model was developed. This model easily computes the electrical power generated by a TEG considering the contact resistivities beside the thermoelectric material properties and the generator geometry. This model is composed of two un-coupled sub-circuits. The thermal sub-circuit, depicted in Figure 3(a), computes the effective temperature difference between the extremities of the thermoelectric legs, ΔT_{teg}. In this subcircuit, the thermal resistance of the thermoelectric leg, Θ, and the thermal contact resistance, Θ_c, in K.W^{-1}, are defined by Equations (3) and (4), respectively:

$$\Theta = \frac{l}{kA} \tag{3}$$

$$\Theta_c = \frac{r_{sc}}{A} \quad (4)$$

l being the thermoelectric leg length, A being the thermoelectric leg area, k is the mean thermoelectric material thermal conductivity in $W.m^{-1}.K^{-1}$ and r_{sc} is the thermal contact resistivity in $K.m^2.W^{-1}$. From the definition of these resistances and knowing the temperature difference between the heat source and sink, ΔT, the effective temperature difference on the thermoelectric legs can be computed as:

$$\Delta T_{teg} = \Delta T \frac{\Theta}{2\Theta_c + \Theta} \quad (5)$$

Equation (5) can be rewritten to describe the relative temperature difference as a function of the thermal parameters:

$$\frac{\Delta T_{teg}}{\Delta T} = \frac{1}{1 + 2\frac{r_{sc}k}{l}} \quad (6)$$

The electrical sub-circuit, depicted in Figure 3(b), is used to estimate the electrical power generated by the TEG. The total TEG resistance is defined as:

$$R_{teg} = R_p + R_n + 4R_c = \frac{\rho_p l}{A} + \frac{\rho_n l}{A} + 4\frac{\rho_{sc}}{A} \quad (7)$$

ρ_p *and* ρ_n being the thermoelectric materials electrical resistivities in Ω.m and ρ_{sc} being the electrical contact resistivity in $\Omega.m^2$. The open circuit thermoelectric voltage can be computed from ΔT_{teg} and $\sum_{mat}$ using Equation (2).

Knowing R_{teg} and V_{oc}, the electrical power at matched load, P_{max}, can be computed as:

$$P_{max} = \frac{V_{oc}^2}{4R_{teg}} \quad (8)$$

Using Equation (2), the power can be expressed as:

$$P_{max} = \frac{(\sum_{mat} \Delta T_{teg})^2}{4R_{teg}} \quad (9)$$

The present model assumes temperature independent properties and neglects the physical coupling occurring through the Joule, Peltier and Thomson effects. These strong assumptions are valid for a first order approximation [27].

RESULTS

Microstructure of the joints

The interface of Fe_2VAl assembled to Cu with silver glue is shown in Figure 4. Silver particles and the epoxy matrix can be discriminated, showing that the conductive phase does not completely fill in the joint between Fe_2VAl and Cu. It is also worth noting that the silver glue layer has a width in the range of 10 to 20 µm.

Figure 5 shows the interface of the assembly using the tin solder. The global shape of the tin solder suggests a very good wetting of Cu, but on the contrary no wetting of Fe_2VAl. It explains the discontinuity of the interface between Fe_2VAl and solder and the bad contact resistivity reported in next section as well as the weak mechanical strength. Indeed, Figure 6 shows the Fe_2VAl soldered sample after disassembling of the Cu-Fe_2VAl joint. It is straightforward when looking at Figure 6(a) that the tin solder joint is quite ineffective. The major part of the surface is free of solder. Moreover, there are some zones free of tin solder inside the solder droplet leading to an even smaller effective contact surface as it is highlighted at higher magnification (see Figure 6(b)).

Figure 7(a) shows the complete Fe_2VAl - Cu interface when joined with silver braze. It can be observed that only one third of the total interface is really connected by the braze. On the other hand, when zooming on the interface, it is clear that the braze reacts with copper. On the Fe_2VAl side, there does not seem to have any reactivity at this scale. The profile of chemical composition of Figure 7(b) highlights that the reactive layer on the Cu side is composed of 70 at.% Cu, 20 at.% Zn and up to 10 at.% Ag. This composition is similar to the one of the Cu-rich particles present in the braze joint. Figure 8 shows the Fe_2VAl surface after disassembling the specimen. It can be seen on Figure 8(a) that the surface is still mostly covered by the silver braze. This is even clearer at higher magnification as shown on Figure 8(b). This could indicate that there is some reaction between the braze and the Fe_2VAl, but a reaction layer could not be observed in this work.

Figure 9 presents a SEM micrograph and an EDX profile of the diffusion bonded joint. The micrograph of Figure 9(a) shows the presence of a thin zone where copper reacts with Fe_2VAl. When zooming, it clearly appears that diffusion of copper occurred along the Fe_2VAl grain boundaries close to the interface. The chemical profiles of Figure 9(b) show that the bright grey zone at the interface is depleted in aluminium. This depleted zone is about 5 µm with some copper particles that are located in this zone. The profile shows that aluminium also diffused within the copper layer.

Characterisation of the electrical contact

The measured electrical contact resistivities are presented in Figure 10 for the different joining techniques. The electrical contact resistivity varies in a very large range depending on the joining process, ranging from 9.46 10^{-6} Ω.m² for the silver glue down to 5 10^{-9} Ω.m² for the silver braze and the diffusion bonded copper.

Prototypes

Table II summarises the experimentally determined electrical characteristics (R_{meas} and Σ_{meas}) as well as the calculated ones (R_{mat} and Σ_{mat}; the '$-mat$' subscript relating to the material properties) estimated based on the prototypes geometry and the materials properties. These characteristics are the ones expected in absence of contact resistances. The measured internal resistance decreases drastically from 40000 mΩ for the Ag glue prototype down to less than 50 mΩ for the Ag braze and diffusion bonded Cu prototypes, while the effective Seebeck coefficient varies from a factor around 5. This is mainly due to the fact that the internal resistance is directly linked to the electrical contact resistance that can significantly varies with the joining techniques (see previous section), while the effective Seebeck coefficient is not directly linked to the electrical contact resistance.

DISCUSSION

Joining processes

Högblom *et al*. reported electrical contact resistivities in the range of $10^{-9} - 10^{-7}$ Ω.m^2 for TEG depending on the process [10]. Most of the techniques used in this work are thus in the range of good performances except for the tin solder and definitely for the silver glue.

The large contact resistivity of the silver glue cannot be explained by its bulk resistivity (~2µΩm) nor the presence of large porosity (see Figure 4). A Cu to Cu joining test was carried out using the same conditions and a low contact resistivity of 3.5 10^{-9} Ωm² was measured. Therefore, the origin of the large contact resistivity probably results from the silver glue – Fe_2VAl interface. The presence of a very thin layer of alumina on the Fe_2VAl could explain this large contact resistivity as it is reported by Weidler *et al.* in the case of aluminium-silver glue contacts [22].

In the case of the tin solder, Ebling *et al*. reported a similar contact resistivity (up to 1.72 10^{-8} Ω.m^2) for soldering tests of Bi_2Te_3 with a Sn-Ag-Cu solder [9]. This level of contact resistivity could be explained by the low wetting behaviour and the weak strength of the joint between Fe_2VAl and tin solder (Figures 5 and 6).

The process leading to the smallest contact resistivity (diffusion bonding) brings about a specific reactivity and the creation of a smooth interphase transition between Fe_2VAl and Cu. In this process, diffusion of the aluminium in the copper has been highlighted. This can be explained by two phenomena: (i) aluminium presents the largest diffusion coefficient; (ii) looking at the phase diagrams of the Al-Cu, Fe-Cu and V-Cu couples, Al presents a large solubility in Cu [28], indicating a good chemical affinity between these two elements.

Figure 10 also showed that silver brazing exhibits electrical contact resistivity similar to copper diffusion bonding (in the 10^{-9} Ω.m^2 range). When comparing the interface of the tin solder test (Figure 5) and the silver brazing test (Figure 7b), it is obvious that the silver braze presents a lower contact angle on Fe_2VAl than the tin solder, which could indicates a better wetting of the silver braze. That could explain a lower contact resistivity even if there is large porosities in the silver braze joint and the bulk resistivities of the filler materials are similar (about 10^{-7} Ω.m). Indeed, the contribution of the silver braze (considering that one third of the area is effectively joined) is around 5.5 10^{-11} Ω.m^2. That is still two orders of magnitude lower than the measured electrical contact resistivity. The better joining behaviour of silver braze compared to tin solder is also confirmed when looking at the disassembled surfaces (Figures 6 and 8). Indeed, the Fe_2VAl surface covered with silver braze is much larger than in the case of tin solder.

Considering the contact resistivities and the easiness of implementation, silver brazing and diffusion bonding seem the most suitable techniques for the development of effective prototypes.

Assembly of the prototypes

Based on the theoretical and experimental values and taking into account the geometrical configurations of the different prototypes, the three contact parameters presented in Table III can be estimated:

- **The mean electrical contact resistivity**, ρ_{sc}, can be computed in the case of a prototype using the following formula:

$$\rho_{sc} = \frac{(R_{meas} - R_{mat})}{4N} A \tag{10}$$

  where A is the thermoelectric leg area and N is the number of thermoelectric couples in the prototype. The factor 4 is due to the number of contacts per couple (2 per leg).

- **The Seebeck ratio**, Σ_{ratio}, defined as [25]:

$$\sum_{ratio} = \frac{\sum_{meas}}{\sum_{mat}} \tag{11}$$

- **The thermal contact resistivity,** r_{sc}, can be computed by using the Seebeck ratio. From Equations (2), (6) and (11), it can be written as:

$$\sum_{ratio} = \frac{\Delta T_{teg}}{\Delta T} = \frac{1}{1+2\frac{r_{sc}k}{l}} \tag{12}$$

Rewriting this equation, the thermal contact resistivity can be expressed as:

$$r_{sc} = \left(\sum_{ratio}^{-1} - 1\right)\frac{l}{2k} \tag{13}$$

It is worth noting that the thermal conductivity of the thermoelectric material and the thermoelectric leg length must be known. A mean thermal conductivity of 12.5 $W.m^{-1}.K^{-1}$ taken from the literature [29] is used for the Fe_2VAl samples processed in this work.

Σ_{ratio} is dependent on the geometry. Indeed, longer thermoelectric legs bring an increase of this ratio for the same thermal contact resistance. This means that it can only be used to compare TEG presenting the same geometry. On the other hand, electrical and thermal contact resistivities are independent of the geometry of the module and can be used to compare different prototypes. For the sake of comparison, the characteristics and performances of two Fe_2VAl-based modules reported in the literature (work of Mikami *et al.* on Ti, Si and W doping [20,21]) are also indicated in the two last rows of Table III.

The mean electrical contact resistivity values determined on the prototypes are in fair agreement with those measured previously during the characterisation of the individual joints (Figure 10). Only in the case of the silver glue, an overall value significantly higher (about 176%) than that of the single test is obtained. Hence, except in the latter case, all prototypes exhibit good electrical contact resistivity in the range of values reported in the literature ($10^{-9} - 10^{-7}$ Ω.m²) [10]. When looking at the electrical contact resistivities of the two last prototypes, it is obvious that the use of silver braze ensures a low electrical contact resistivity. Thereupon, the diffusion bonded prototype presents nearly the same electrical contact resistivity than the silver braze prototype, confirming that the Cu - Fe_2VAl joints present an ultra-low resistivity.

To highlight the contribution of the silver braze in this assembly, a copper-to-copper joint has been silver brazed. The measured contact resistivity was 1.7 10^{-9} $\Omega.m^2$. This represents about 40 % of the total surface contact resistivity of the Fe_2VAl/Cu/Braze/Cu assembly. This conclusion is confirmed when looking at the two state-of-the-art prototypes from Mikami *et al.* that exhibit an electrical contact resistivity one order of magnitude lower than in this work [20, 21]. This lower contact resistivity probably results from the fact that they manufactured the prototypes only by SPS (without an additional brazing step). Further work on this process scalability and on the resulting mechanical properties should be considered.

The Seebeck ratio, Σ_{ratio}, of all prototypes is in the range of 0.4-0.7, which is comparable to other works (see Table III). As defined in Equation 12, this ratio depends on the thermal contact resistance and the thermal resistance of the thermoelectric leg. Therefore, a higher Seebeck ratio will be obtained when lowering the thermal contact resistivity, the thermoelectric leg thermal conductivity and when increasing the thermoelectric leg length. These effects are highlighted when comparing the silver glue prototype with the others (see Table III).

For the thermal contact, the first prototype presents the lowest thermal contact resistivity. This could be explained by the fact that the silver glue prototype was assembled between the heater and the heat sink used for the characterisation before the curing step. Therefore, the planarity could have been improved compared to other modules leading to a lower thermal contact resistance. A typical thermal contact value of about 2 10^{-4} $K.m^2.W^{-1}$ is found for the other prototypes. This value is similar to the one found by Hogblöm *et al.* for commercial bismuth telluride modules [10].
Finally, the two state-of-the-art prototypes from Mikami *et al.* present similar thermal contact characteristics than the present work [20, 21]. This could indicate that the thermal contacts are dominated by the interface (anodised aluminium and thermal grease in this work) between the copper plates and the heat source and sink rather than by the interface between copper and thermoelectric materials.

Several performances indexes of the prototypes were computed from the previous measurements. In order to compare the different prototypes, together and with respect to the literature, Table III presents these characteristics:

- P_{max}, the power at matched load for a 200 K temperature difference. It is estimated as:

$$P_{max} = \frac{(\Sigma_{meas} \Delta T)^2}{4R_{meas}} \quad (14)$$

- $p_{max/mat}$, the resulting power density on the thermoelectric material area.
- $p_{max/tot}$, the resulting power density on the total area of the prototype.

Figure 11 presents the electrical contact resistivity, the thermal contact resistivity and the total power density for the different prototypes and for those reported in the literature. From this graph, it is clear that the dramatic decrease of the electrical surface contact resistivity thanks to an optimisation of the joining process leads to a sharp increase of the power density.

It is worth noting that the best prototype of the present study presents similar performances than the Si/Ti doped module of Mikami *et al.* which can be considered as the best results ever reported for TEGs based on Fe_2VAl. However, the present prototype is the first one based on off-stoichiometric Fe_2VAl

compounds. Furthermore, similar performances are reached even with higher ρ_{sc}. Moreover, skipping the use of doping elements and avoiding the powder metallurgy route allows one to produce modules faster and at a lower cost. Moreover, when comparing this work with the literature, it can be observed that the relative difference between $p_{max/mat}$ and $p_{max/tot}$ is much smaller in the present work than in the work of Mikami *et al.* [20, 21]. This indicates that the geometry used in this work is closer to an optimal geometry.

Optimisation based on the lumped model

The influence of contact resistances on the delivered power can be highlighted using the lumped model. An example for ΔT = 200 K using Fe_2VAl as the thermoelectric material has been computed. Figure 12 shows the ratio of the real power to the ideal power (without contacts) as a function of the electrical contact resistivity and also for different levels of thermal contact resistivity. The different curves increase up to a maximum when electrical contact resistivity is minimised. Even though this parameter was not the topic of the optimisation procedure in the present study, the thermal contact resistivity should be minimised too, since the smaller the thermal contact resistivity, the larger the power, whatever the value of the electrical contact resistivity.

Finally, the successive improvements in the prototype design allowed to increase the power density by a factor of about 4000 owing to a sharp decrease of the electrical contact resistivity (about 4 orders of magnitude). This sharp increase is clearly in agreement with the model presented at the beginning of this work as depicted in Figure 12. In this figure, the experimental data (red dots) well agree with the lumped model (discontinuous line) computed using the mean values of prototypes characteristics (l = 4.45 mm, ρ = 5 µΩ.m, S_p=|S_n|= 64.25 µV.K^{-1}).

Since the goal of the generator design should be to reach a ratio p/p_{ideal} as close as possible from 1, it can be stated that the optimisation of electrical contacts made in this work is close to its best. However, there is still room for improvement by optimising the thermal contacts. Moreover, since this work focuses only on the influence of the assembly process on the prototype performances, a further increase of the performances can be obtained through a geometrical optimisation.

Selection of the joining process

After the selection of the appropriate metal electrode (thermal expansion matching, chemical and mechanical stability at working temperature…), this global study can be used to define the selection procedure of a joining process for new thermoelectric materials. The flowchart of this procedure is given in Figure 13 and contains the following steps:

1. **To select a joining process that leads to a good metallurgical bond**: A good wetting and a thin reaction layer should appear during joining even though diffusion must be avoided at working temperature. Basic principles of physical chemistry and metallurgy compiled in tools like phase diagrams, chemical affinity and microstructural characterisation of the joint interface are the first required steps.
2. **To perform a joining test**: Tests on single leg samples should be used to find the joining conditions that lead to a small electrical contact resistivity. A measurement setup for the electrical contact characterisation is required as well as the model to estimate the performances.
3. **To assemble a multicouple working prototype**: The prototype should validate the upscaling of the joining technique considering manufacturing and performances issues. The prototype should be fully characterised in terms of thermal and electrical contacts and performances.

It is mandatory that the different steps are fully completed to validate the choice of a joining process for the development of thermoelectric generators using new thermoelectric materials. Therefore, the whole selection process should be taken into account when developing a joining process. Indeed, choosing a process that does not complete the three steps will definitely not lead to a high performance generator. This bad choice is clearly highlighted by the silver glue example in this study where no metallurgical bond occurred leading to bad performances. On the opposite, a good joining technique leading to good contact on single leg samples could be developed but fail to pass the upscaling stage towards the prototype assembly step by being too complex.

CONCLUSION

Thermoelectricity is a promising technology to change the way low grade heat is considered. However, there is still room for improvement to bring this technology closer of real applications. Especially, thermal and electrical contacts should be minimized in TEGs to fully use the potential of thermoelectric materials. This work proposes a global assessment of these contacts.

The first order lumped model described in this work allows easily estimating the electrical power of a TEG considering the thermal and electrical contact resistivities. This model has been used to highlight the influence of contact resistivites on the electrical power density. The results show that these contacts must be minimised to maximise the power density.

Based on the Fe_2VAl thermoelectric compound, a global analysis of the metal-to-thermoelectric material assembly has been accomplished. This analysis showed that assembly techniques leading to a reaction layer between the metal and the thermoelectric material give the lowest electrical contact resistivities.

Using these assembly techniques, several TEG prototypes have been manufactured and characterised. The power density of the prototypes has been dramatically increased through the use of the best assembly techniques (a factor 4000 from the silver glue to the diffusion bonded copper technique). Furthermore, these Fe_2VAl-based TEGs using the off-stoichiometry doping route compete with the Si/Ti doped prototypes [20] with a power density larger than 500 $W.m^{-2}$ for a temperature difference of 200 K.

Future work should focus on the simultaneous minimisation of the thermal and electrical contact resistivities in parallel to the development of high performance low-cost and easily manufacturable thermoelectric materials. The selection process resulting from this study is a simple and powerful tool to speed up this development.

Acknowledgements

Authors acknowledge the support of the Walloon Region through the funding of the GTherm project. The European Regional Development Fund (ERDF) and Wallonia, are also gratefully acknowledged for their financial support of the research project (T-REX– EQUIDER - ECV12020010884F-830033) in the frame of the “Convergence programme".

REFERENCES

1. Liu, W., Jie, Q., Kim, H. S., and Ren, Z. *Acta Mater*, *87*, 357 (2015).
2. Rowe, D. M., and Min, G.. *IEE Proc-A*, *143*, 351(1996).
3. Liu, W., Wang, H., Wang, L., Wang, X., Joshi, G., Chen, G., & Ren, Z. *J Mater Chem A*, 42, 13093 (2013).
4. de Boor, J., Gloanec, C., Kolb, H., Sottong, R., Ziolkowski, P., & Müller, E. *J Alloy Compd*, *632*, 348 (2015).
5. Zhao, D., Geng, H., & Chen, L. (2012). *Int J Appl Ceram Tec*, *9*, 733 (2012).
6. Ziolkowski, P., Poinas, P., Leszczynski, J., Karpinski, G., & Müller, E. (2010). *J Electron Mater*, *39*, 1934 (2010).
7. Bjørk, R. *J Electron Mater*, *44*, 2869 (2015).
8. Reddy, B. V. K., Barry, M., Li, J., & Chyu, M. K. *J Heat Transf*, *136*, 101401 (2014).
9. Ebling, D., Bartholomé, K., Bartel, M., & Jägle, M. *J Electron Mater*, *39*, 1376 (2010).
10. Högblom, O., and Andersson, R. *J Electron Mater*, *43*, 2247 (2014).
11. Fateh, H., Baker, C. A., Hall, M. J., & Shi, L. *Appl Energ*, *129*, 373 (2014).
12. Ngan, P. H., Van Nong, N., Hung, L. T., Balke, B., Han, L., Hedegaard, E. M. J., Linderoth, S., and Pryds, N. *J Electron Mater*, *45*, 594 (2016).
13. Roy, G., Matagne, E., and Jacques, P. J. *J Electron Mater*, *42*, 1781 (2013).
14. Nishino, Y., Kato, H., Kato, M., and Mizutani, U. *Phys Rev B*, *63*, 233303 (2001).
15. Nishino, Y., and Tamada, Y. *J Appl Phys*, *115*, 123707 (2014).
16. Miyazaki, H., Tanaka, S., Ide, N., Soda, K., and Nishino, Y. *Mater Res Express*, *1*, 015901 (2014).
17. Mikami, M., Kinemuchi, Y., Ozaki, K., Terazawa, Y., and Takeuchi, T. *J Appl Phys*, *111*, 093710 (2012).
18. Renard, K., Mori, A., Yamada, Y., Tanaka, S., Miyazaki, H., and Nishino, Y. *J Appl Phys*, *115*, 033707 (2014).

19. van der Rest, C. PhD Thesis, Université catholique de Louvain (2015).
20. Mikami, M., Kobayashi, K., Kawada, T., Kubo, K., and Uchiyama, N. *J Electron Mater*, *38*, 1121 (2009).
21. Mikami, M., Mizoshiri, M., Ozaki, K., Takazawa, H., Yamamoto, A., Terazawa, Y., & Takeuchi, T. *J Electron Mater*, *43*, 1922 (2014).
22. Weidler, J. D., Burg, R. D., Decker, J. J., & Constable, J. H, in *Proceedings of Electronic Components and Technology Conference* (2000), pp. 906-913
23. Shiue, R. K., Li, Y., Wu, S. K., and Wu, L. M. *Metall Mater Trans A*,*41*, 2836 (2010).
24. Brochu, M., Pugh, M., and Drew, R. A. L. *Intermetallics*, *12*, 289 (2004).
25. Huang, G. Y., Hsu, C. T., and Yao, D. J. *J Electron Mater*, *43*, 2337 (2014).
26. Hsu, C. T., Huang, G. Y., Chu, H. S., Yu, B., and Yao, D. J. *Appl Energ*, *88*, 5173 (2011).
27. Freunek, M., Müller, M., Ungan, T., Walker, W., and Reindl, L. M. *J Electron Mater*,*38*, 1214 (2009).
28. H.Okamoto, M.Schlesigner, and E.Mueller, ASM Handbook Volume 3: Alloy Phase Diagrams (ASM International,1992).
29. Lue, C. S., Chen, C. F., Lin, J. Y., Yu, Y. T., and Kuo, Y. K. *Phys Rev B*, *75*, 064204 (2007).

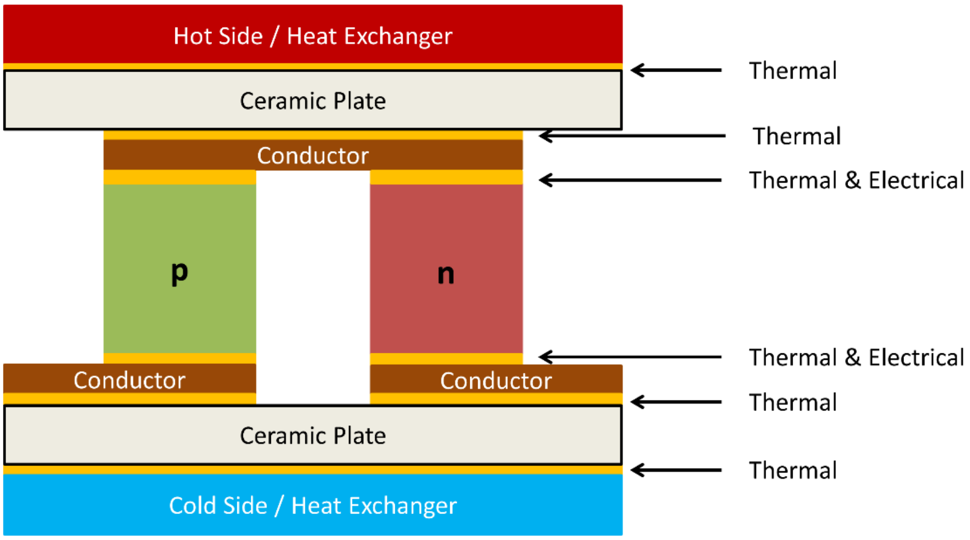

Fig. 1. Localisation of thermal and electrical contacts in a thermoelectric couple.

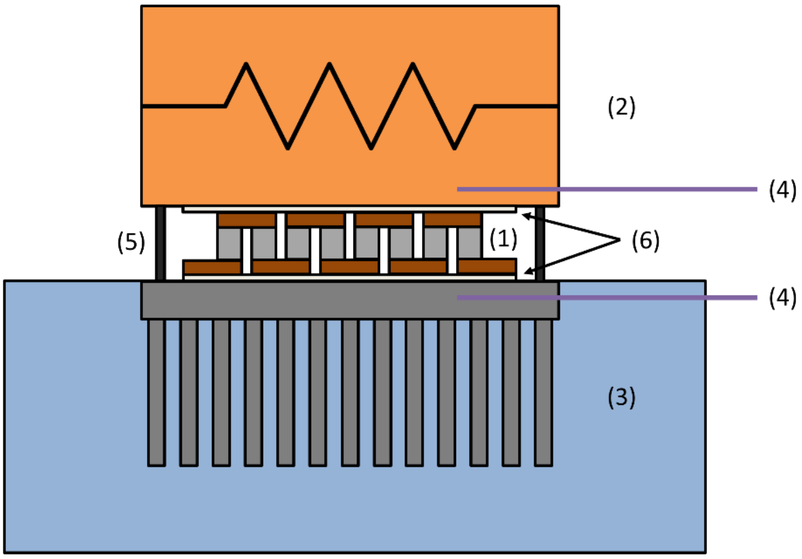

Fig. 2. Schematic representation of the custom setup used for the characterisation of the modules. 1, module; 2, heater sheeted with anodised aluminium; 3, heat sink made of anodised aluminium immerged in a cooled propanol bath; 4, thermocouples; 5, clamping screws; 6, thermal grease layers.

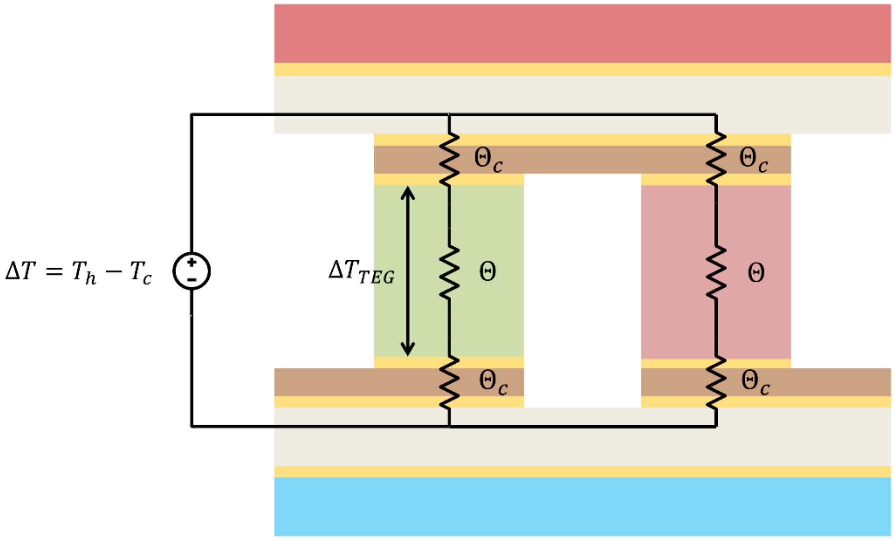

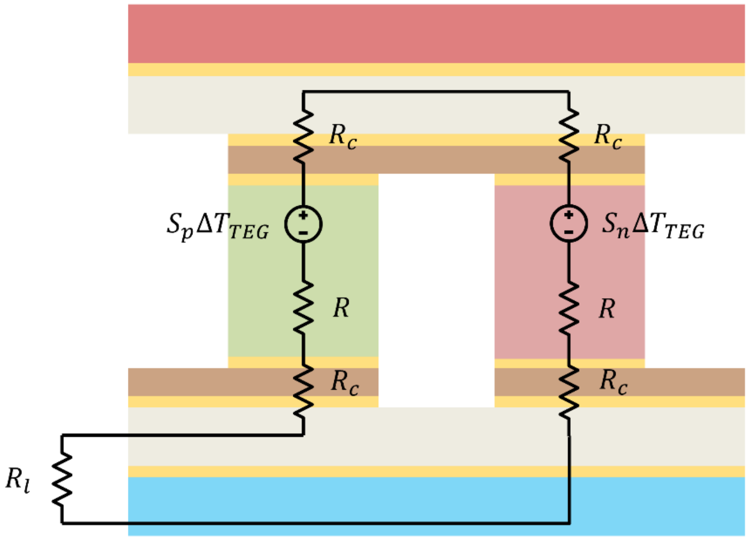

Fig. 3. (a) Description of the thermal lumped model. (b) The electrical lumped model used to assess the properties of the prototypes.

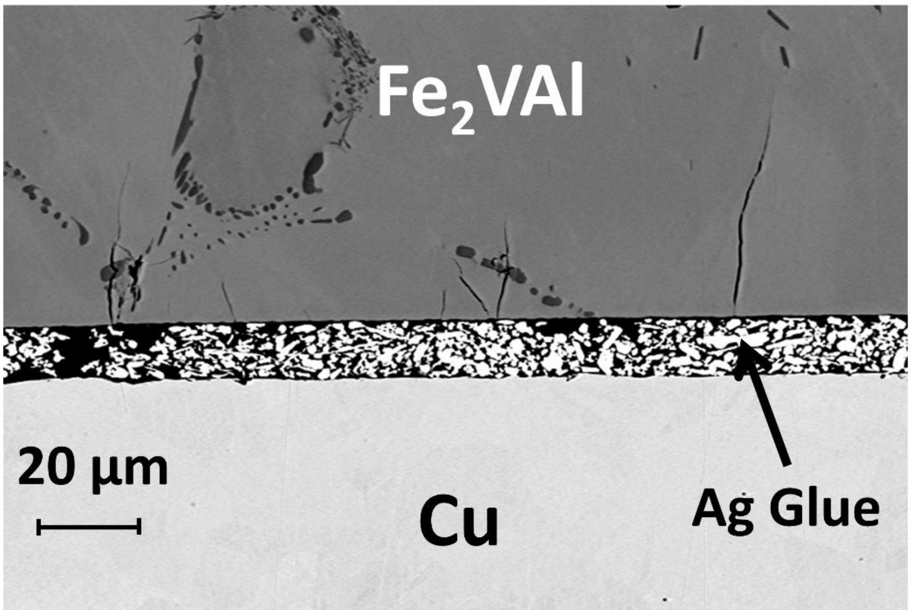

Fig. 4. Micrograph of a cross-section of the Fe_2VAl - silver glue – Cu assembly.

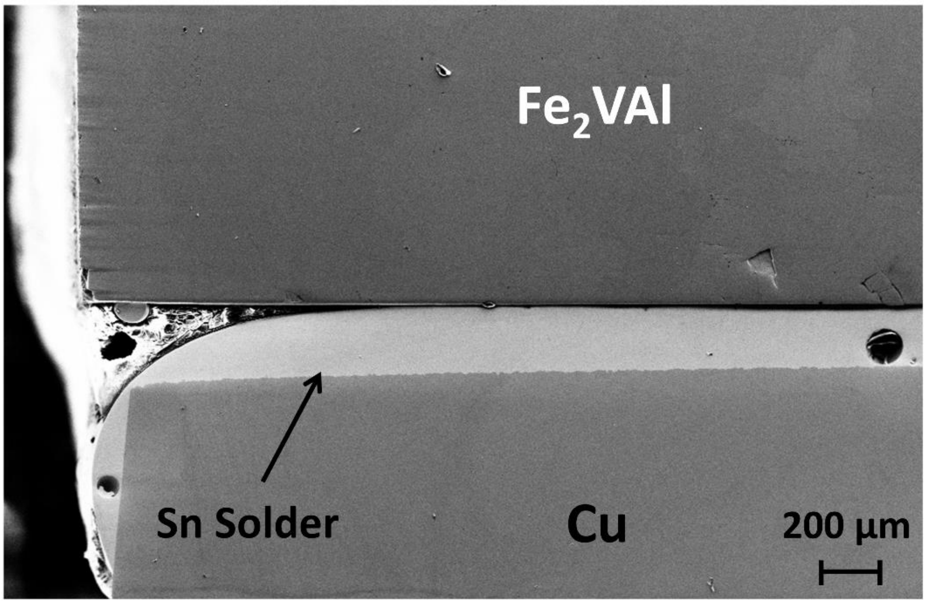

Fig. 5. Micrograph of a cross-section of the Fe_2VAl - tin solder – Cu assembly.

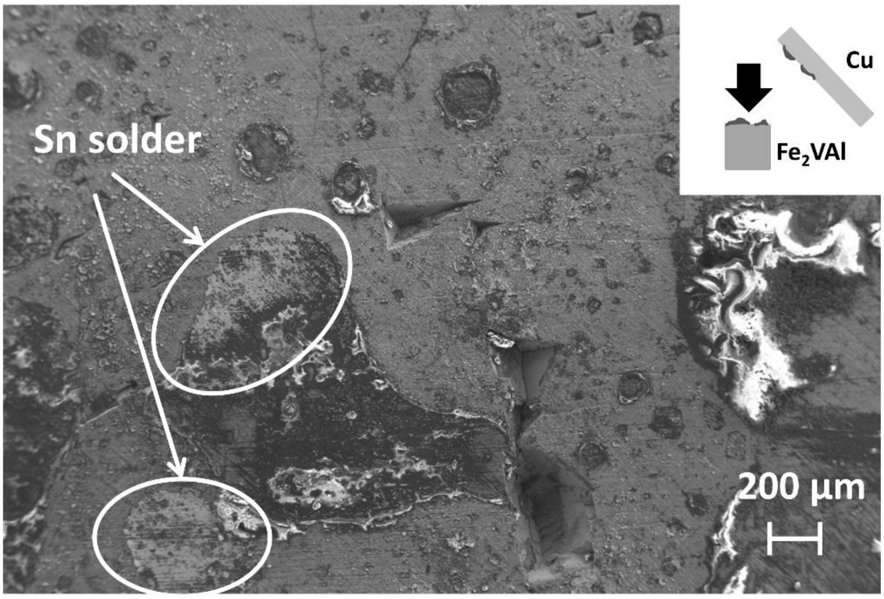

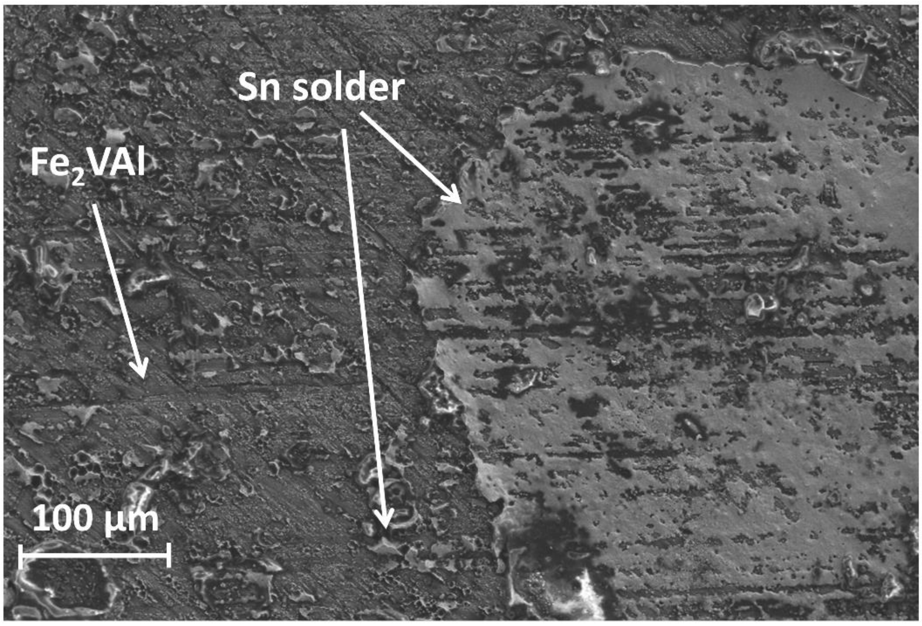

Fig. 6. (a) Micrograph of the Fe_2VAl surface after disassembling the tin soldered specimen. (b) Magnified view on a tin droplet of Figure 6a.

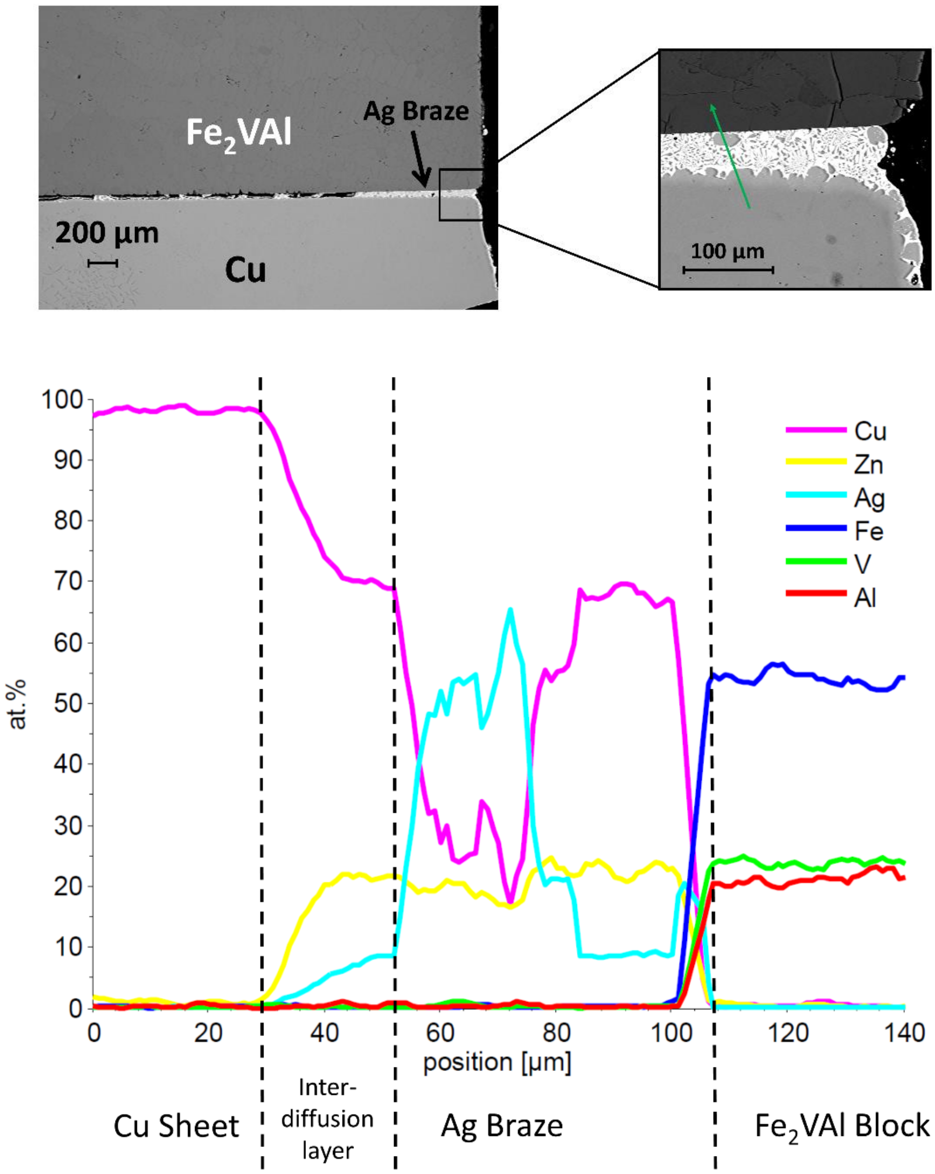

Fig. 7. (a) Micrograph of a silver brazing test. (b) EDX chemical interface profile following the green arrow in Figure 7a.

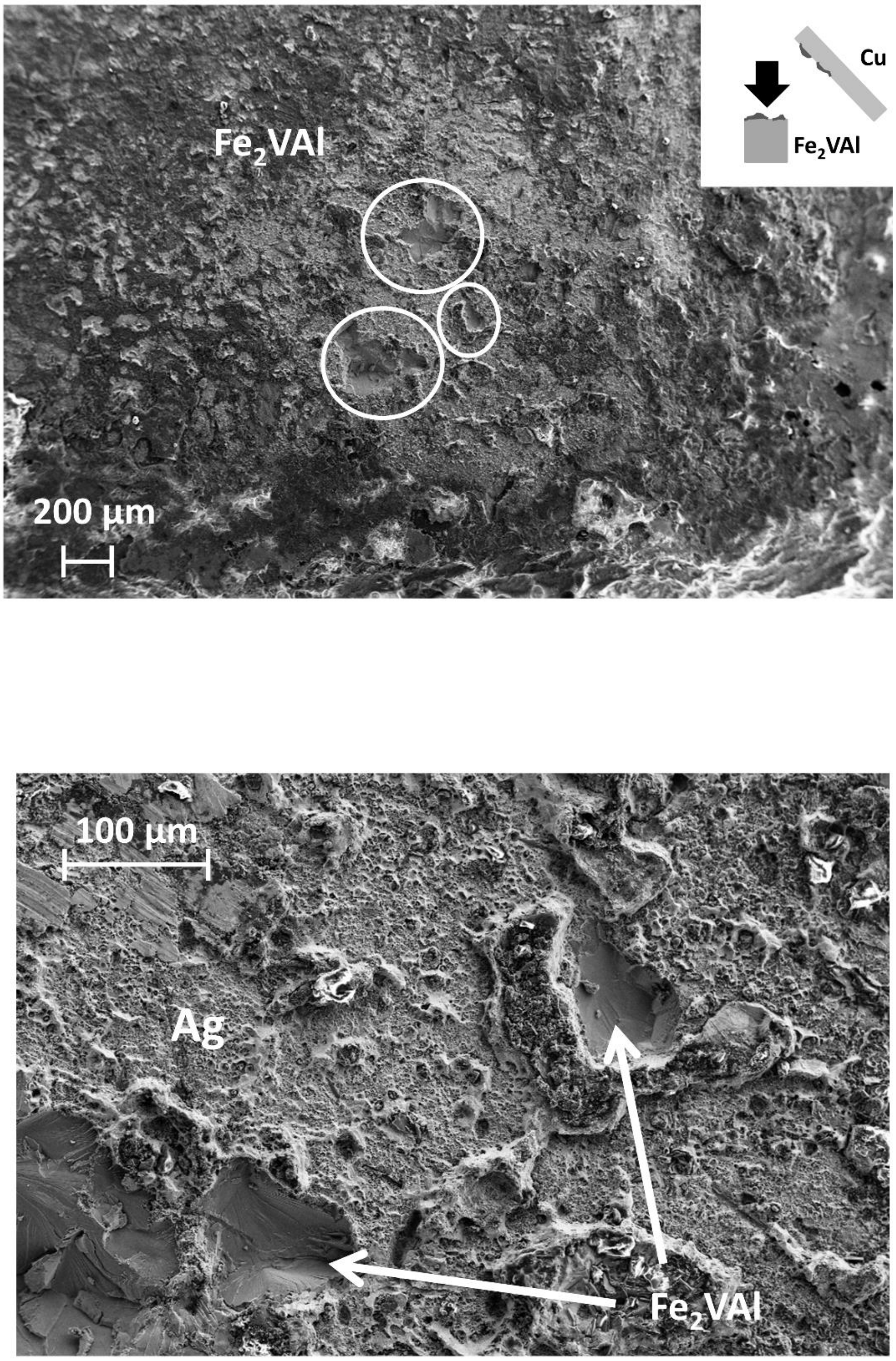

Fig. 8. (a) Micrograph of the Fe_2VAl surface after disassembling the silver brazed specimen. (b Magnified view on the silver-free-zone in Figure 8a.

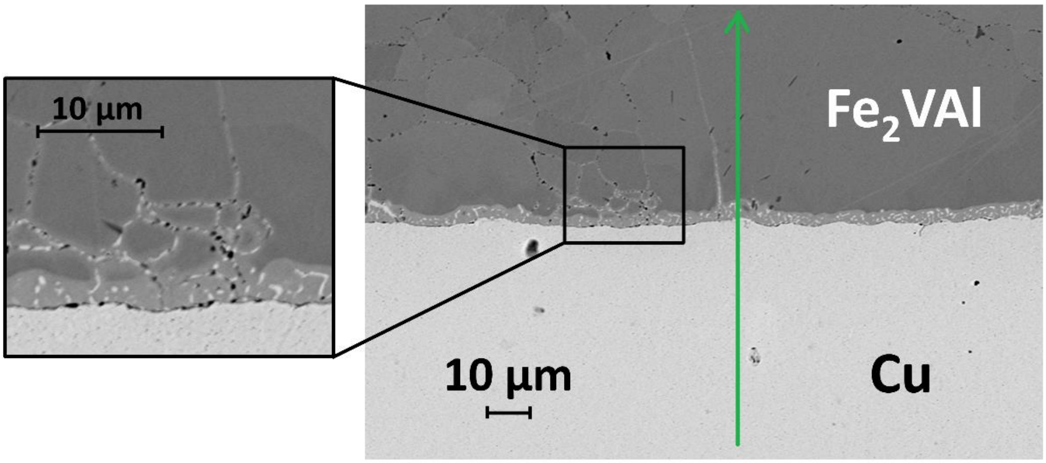

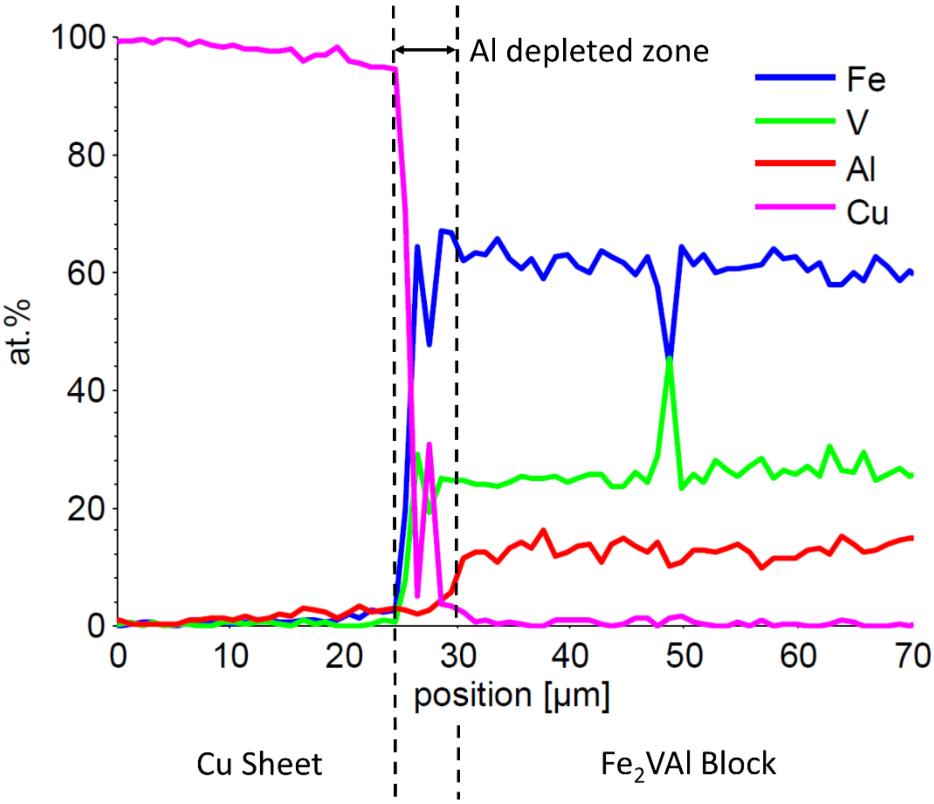

Fig. 9. (a) Micrograph of the interface of the diffusion bonding test. (b) EDX chemical interface profile following the green arrow in Figure 9a.

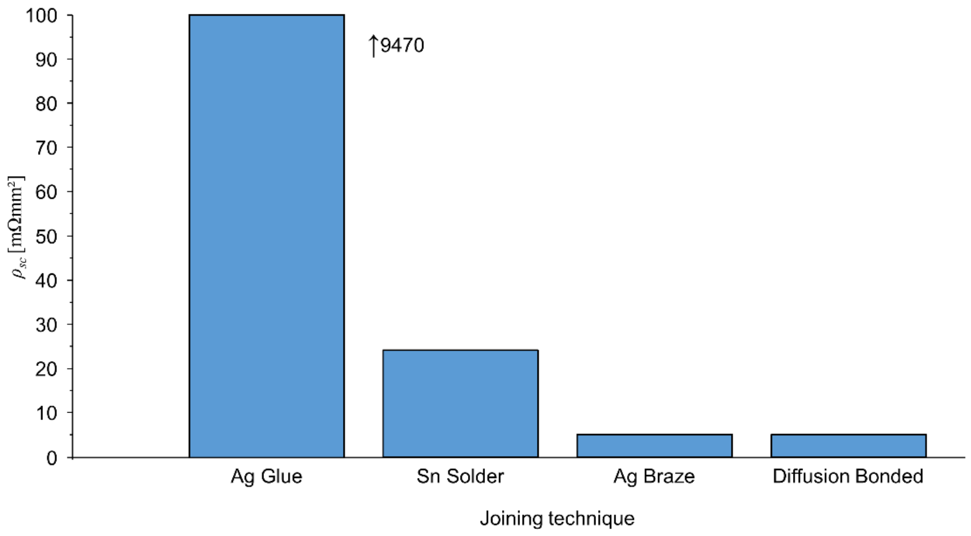

Fig. 10. Surface electrical contact resistances measured during joint testing for four different joining techniques.

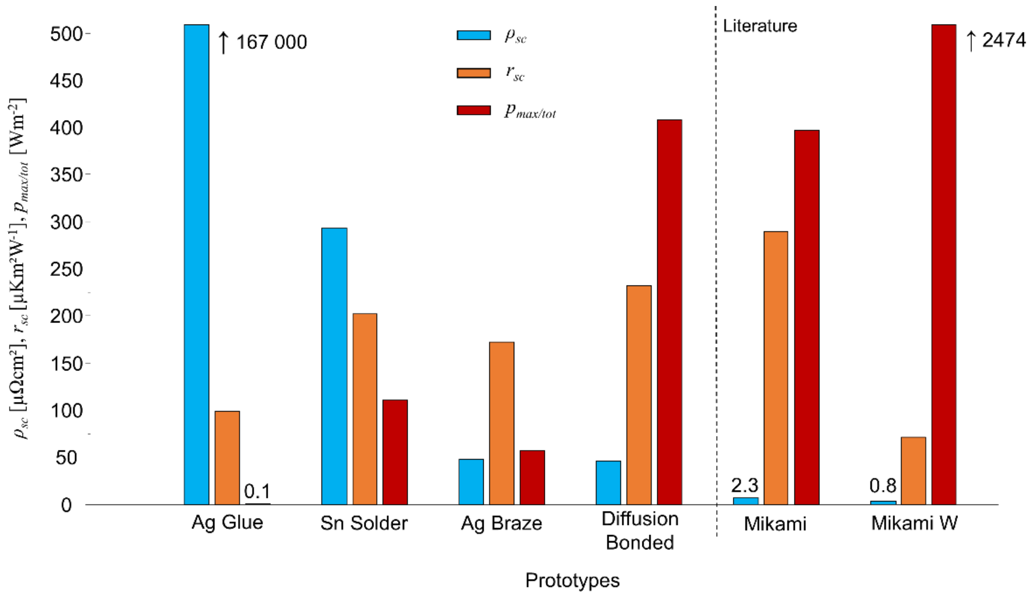

Fig. 11. Performances and contact characteristics of the prototypes. The blue bars depict ρ_{sc} in μΩ.m², the orange bars depict r_{sc} in μK.m².W^{-1} and the red bars depict the total power density in W.m^{-2}. The characteristics of two prototypes were estimated using data from the literature for the sake of comparison: A Si/Ti-doped ("Mikami", from [20]) and a W-doped ("Mikami W" from [21]).

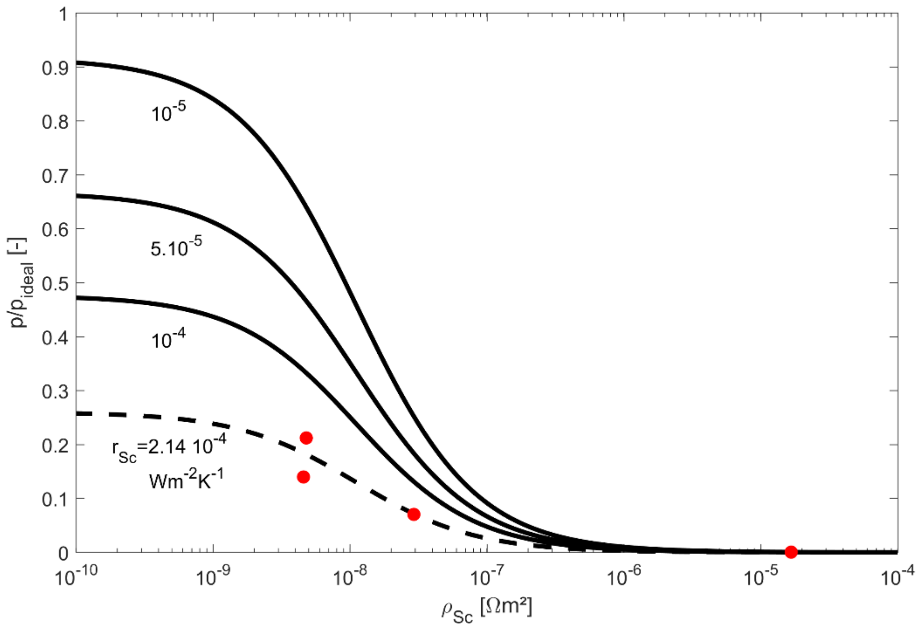

Fig. 12. Normalised power as a function of electrical surface contact resistivities for different levels of thermal surface contact resistivites. The red dots correspond to the different prototypes manufactured in this work. The black lines are computed with the lumped model using the following characteristics: ΔT = 200 K, l = 4.45 mm, k = 10 W.m^{-1}.K^{-1}, ρ = 5 µΩ.m, S_p=|S_n|= 64.25 µV.K^{-1}. The discontinuous black line is computed using the mean value of the thermal surface contact resistivities of the prototypes.

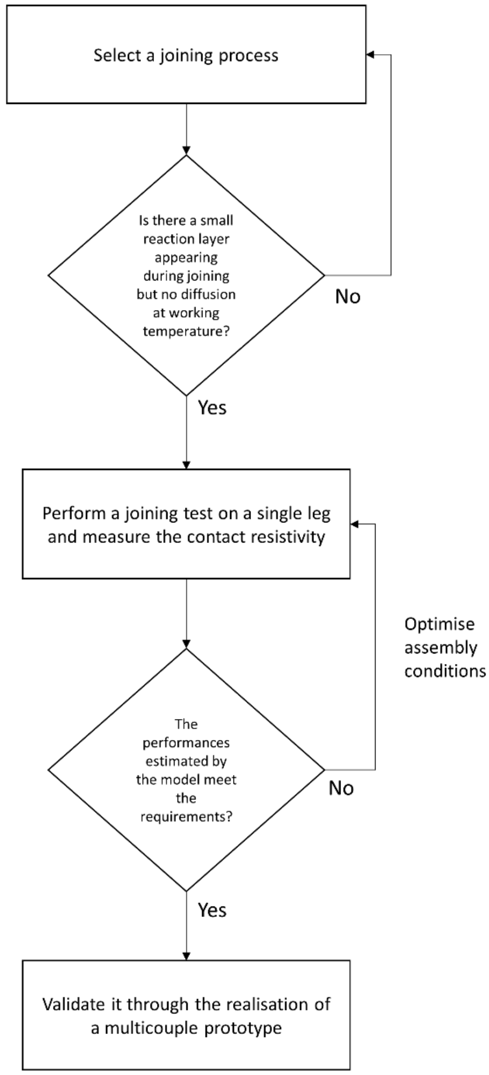

Fig. 13. Flowchart of the selection of the joining technique for high performances TEG.

Table I. Characteristics of the prototypes.

Prototype	*p*-type			*n*-type			Legs size (mm^3)
	Composition	*S* ($\mu V.K^{-1}$)	*ρ* ($\mu\Omega.m$)	Composition	*S* ($\mu V.K^{-1}$)	*ρ* ($\mu\Omega.m$)	
Ag Glue	$Fe_{49.2}V_{24.3}Al_{26.5}$	42	1.47	$Fe_{52.6}V_{25.4}Al_{22.6}$	-20	8.77	5x5x5
Sn Solder	$Fe_{50.9}V_{24.7}Al_{24.4}$	72	4	$Fe_{51.7}V_{26.1}Al_{22.2}$	-70	5.8	4.3x5x5
Ag Braze	$Fe_{50.9}V_{24.7}Al_{24.4}$	72	4	$Fe_{51.7}V_{26.1}Al_{22.2}$	-70	5.8	4.3x5x5
Diffusion bonded	$Fe_{49.3}V_{23.7}Al_{27}$	71	2.32	$Fe_{52.8}V_{26.4}Al_{20.8}$	-97	4.77	4.2x4x4

Table II. Measured properties of the four prototypes.

Prototype	R_{meas} ($m\Omega$)	$\sum_{meas}$ ($\mu V.K^{-1}$)	R_{mat} ($m\Omega$)	$\sum_{mat}$ ($\mu V.K^{-1}$)
Ag Glue	40000	620	30.7	920
Sn Solder	255	2600	67.4	5680
Ag Braze	45	494	32.7	994
Diffusion bonded	48.5	1125	29.8	2688

Table III. Characteristics and performances of the prototypes for ΔT = 200 K.

	Contact Properties			Power Performances		
Prototype	ρ_{sc} (Ω.m²)	$\sum_{ratio}$ (-)	r_{sc} (K.m².W^{-1})	P_{max} (W)	$p_{max/mat}$ (W.m^{-2})	$p_{max/tot}$ (W.m^{-2})
Ag Glue	1.67 10^{-5}	0.67	9.85 10^{-5}	9.61 10^{-5}	0.128	0.107
Sn Solder	2.93 10^{-8}	0.46	2.02 10^{-4}	0.265	132.5	110.41
Ag Braze	4.8 10^{-9}	0.50	1.72 10^{-4}	5.42 10^{-2}	67.75	56.46
Diffusion Bonded	4.58 10^{-9}	0.42	2.32 10^{-4}	0.261	509.77	407.81
Fe_2VAl [20]	3.27 10^{-10}	0.42	2.89 10^{-4}	0.486	687	397
Fe_2VAl W [21]	8.33 10^{-11}	0.75	7.14 10^{-5}	0.715	4965	2474